臨床経験

選択的単一胚移植（eSET）における移植胚選別困難例に対する呼吸量測定の有用性

後藤香里* 小池 恵* 熊迫陽子* 宇津宮隆史* 阿部宏之**

eSETは最も発育能のある胚を見分け移植することが望まれる。移植胚選別において，Day 3の形態評価に呼吸量評価を加えることで発育能のある胚が選別できるか検討した。Day 3の分割別に呼吸量の違いによる胚盤胞到達率を調べたところ，形態評価のみで高率に胚盤胞へ到達する8分割を除いた9分割以上，7，6分割で呼吸量を測ることで胚盤胞到達胚の選別が可能となった。呼吸量が最も大きい胚を移植した場合，形態評価のみの移植と比較して，高い妊娠率と低い流産率が得られた。また呼吸量測定した胚移植で健常な出生を確認した。

はじめに

近年の妊娠率向上，多胎率の上昇に伴い体外受精の移植胚は1個とすることが求められている[1]。着床能のある1個の胚を見分け移植することが望まれるが，移植時に形態が等しく，選別困難である場合も少なくはない。妊娠率を低下させることなく多胎率，流産率を減少させるには，より着床しうる能力を持った1個の胚を選択することが不可欠である。現在，胚の評価は簡単で非侵襲的な方法である顕微鏡下での形態評価のみで行われている。しかし，形態評価は観察者の主観により判定結果に差が生じる可能性があるため，より客観的で精度が高く，安全な胚評価法の開発が望まれている。電気化学計測技術を基盤とする走査型電気化学顕微鏡は受精卵の呼吸活性を非侵襲的に測定することができる。

この細胞呼吸能測定による胚評価法を形態評価に加えることで，最も着床能のある1個の胚を見分けることが可能となるか検討した。呼吸量測定後，出産した症例についての出生結果も報告する。

*Kaori GOTO, Megumi KOIKE, Yoko KUMASAKO, Takafumi UTSUNOMIYA
セント・ルカ産婦人科
**Hiroyuki ABE
山形大学大学院理工学研究科物質化学工学専攻
〒870-0947 大分県大分市津守富岡5組（セント・ルカ産婦人科）

1. 対象および方法

呼吸量測定装置と，測定の概略を示す（図1）。方法は那須らの方法に順じた[2]。

1. 検討1：Day 3（媒精後3日目）の分割数と呼吸量の関係

2006年7月～2009年9月に，Day 3-eSET (elective Single Embryo Transfer)予定となり，移植時Veeckの分類にてグレード1もしくは2である良好胚が2個以上存在し移植胚の選別が困難と思われる307症例574個の胚を対象とした。Day 3に観察した分割数別に，胚呼吸量を調べ，胚盤胞到達率を調べた。測定後移植した胚は今回の検討から除いている。

2. 検討2：eSETにおける検討

2007年3月～2009年9月にVeeckによる形態評価がまったく等しい良好胚が2個以上存在

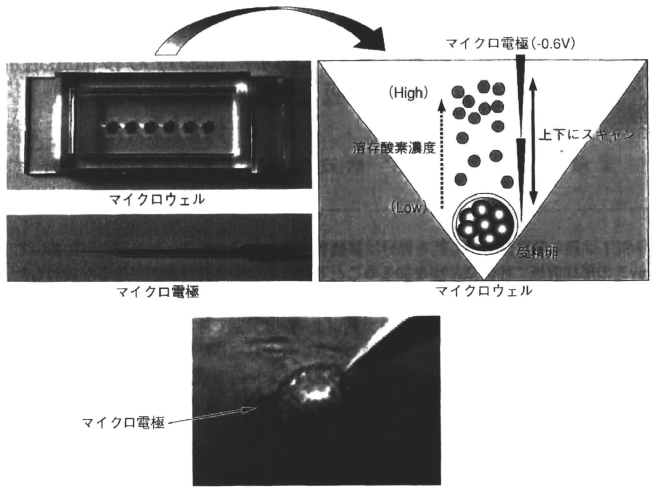

図 1　呼吸量測定の概略

し，Day 3-eSET を行った症例 68 周期を対象とした。前方視的検討として Day 3 の形態がまったく同じ良好胚が 2 個以上存在した場合，移植胚の選択は無作為に呼吸量測定群と形態評価のみの群に振り分け，妊娠率，流産率，継続妊娠率を検討した。

3. 検討 3：出生について

呼吸量評価が高く移植胚となり，出産に至った出生結果を形態評価のみで出産した場合と比較した。

II. 結　果

1. 検 討 1

Day 3 で 9 割球以上に分割していた胚の胚盤胞到達率は呼吸量 $0.3\times10^{14}/mols^{-1}$ 未満で 46.2%，0.3～0.4 未満で 81.8%，0.4～0.5 未満は 66.7%，0.5 以上で 65.5% と 0.3 未満と比較し 0.3～0.4 未満で胚盤胞到達率は高くなる結果を示した（$p<0.05$）。8 分割胚では呼吸量の差による発育の違いは認めなかった（77.1%，70.2%，76.7%，83.3%）（図 2）。

7 分割胚ではどの群にも有意差は認めなかったが，呼吸量が大きくなるに従い胚盤胞到達率が高くなる傾向を示した（50.0%，61.3%，56.0%，69.4%）。6 分割胚ではその傾向も顕著となり，呼吸量 0.3 未満と比べ，0.5 以上で胚盤胞到達率は有意に高くなる結果を認めた（$p<0.05$）（29.4%，38.2%，50.0%，57.1%）（図 3）。

2. 検 討 2

形態評価がまったく等しい良好胚が 2 個以上ある移植胚選別困難例において，呼吸量測定群の妊娠率は 50.0%，形態評価のみの群は 26.5% で呼吸量の大きい胚を移植することにより，高い妊娠率が得られた（$p<0.05$）（図 4）。流産率は呼吸量評価を加えた群で 5.9%，形態評価のみでは 22.2% と呼吸量評価を加えた群で低くなる傾向を示した。継続妊娠率は，従来の形態評価のみでは 20.6% であったのに対し，呼吸量評価を行うことで 47.1% にまで向上した（$p<0.05$）。

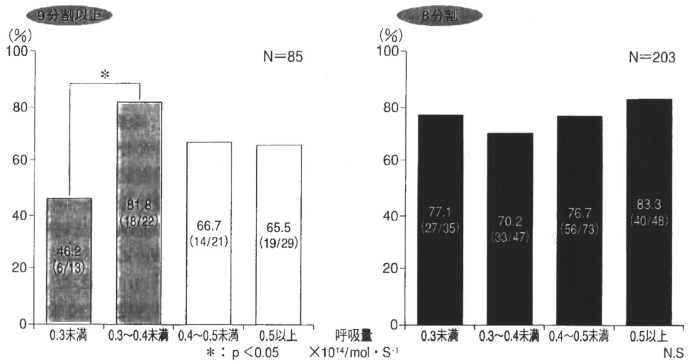

図２　分割数別にみた胚呼吸量と胚盤胞到達率

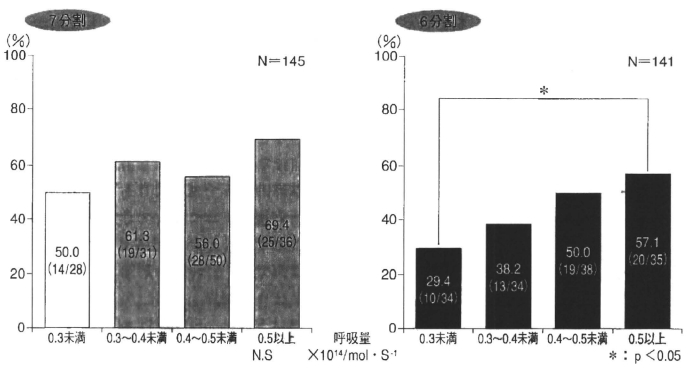

図３　分割数別にみた胚呼吸量と胚盤胞到達率

3. 検討３

現在まで判明しているそれぞれの出生結果を示す。呼吸量評価が高く移植胚となり，妊娠が成立し，出産に至ったのは11名で，男児６名，女児５名，平均体重は2,906 gだった。形態評価のみで出産に至った７名は，男児４名，女児３名，平均体重は2,720 gだった。両群に有意差を認めず，呼吸量測定を行っても健常な出生を認めた。

Ⅲ. 考　察

体外受精が登場して以来，妊娠率向上のため多くの施設で２個以上の胚移植が行われてきた。近年の体外受精技術の発展により，妊娠率は上昇し，それに伴い多胎率の増加も報告されている[1]。体外受精技術を提供しているわれわれにとって，妊娠率を低下させることなく，危険な合併症や周産期異常が危惧される多胎妊娠

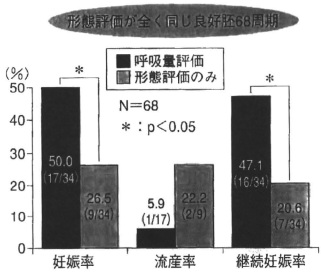

図4　選択的単一胚移植（eSET）の妊娠率

を防ぐことは，重要な課題である。2008年2月，日本産科婦人科学会から条件付きで移植胚は原則1個とするという改定案が出された。このため最も着床能力のある1個の胚を見分けることがさらに要求される。

現在まで妊娠率向上のため多くの研究者より様々な胚の形態評価法が報告された。前核期ではZollnerら[3]，Scottら[4]，Tesarikら[5]が前核の接着や核小体数の評価に基づく判定を提案している。2細胞期胚ではそれぞれの細胞の核の局在判定と早期分割による胚発生能の評価法が提案されている[6]。1998年頃からは，胚の長期培養による選別法が考えられ，胚盤胞期移植が注目されるようになった。分割期と胚盤胞期移植の比較検討では，Gardnerら[7]が，胚盤胞期移植で着床率は有意に上昇したと報告した。しかし，Coskunら[8]やUtsunomiyaら[9]は，胚盤胞まで発育が進まず移植キャンセルとなった症例を含めると，妊娠率は分割期移植と有意差はないという報告もしている。これらの評価法はすべて形態評価であり，観察者の主観によって差が生じる可能性がある。このことからもいまだ決定的な胚の選別方法は確立されていないと考えられる。

阿部らは，細胞活動に必要なエネルギー（ATP）を産生するミトコンドリアの酸化的リン酸化反応（呼吸）に着目した[10][11]。胚の呼吸量を測定することにより，品質評価が可能となるか検討するため，非侵襲的な呼吸測定装置を開発している[12)~14]。これまでに，ウシ，ブタ，マウスの呼吸量解析に成功しており，胚評価への有効性を示した[15]。そこで，われわれはヒト胚への応用を目的に，余剰胚の呼吸量測定を行った。呼吸量測定の安全性を確認するため，呼吸量測定胚および非測定胚において，胚盤胞到達率に差がないか検討したが，両群で差は認めなかった[16]。また，胚の品質と呼吸量の関連性を検討した結果，Veeckの分類法による形態評価は呼吸量と必ずしも一致しないことを示し，呼吸量測定は，形態観察では評価できない胚の状態を数値化して示すことが可能となることを報告した[17]。また，ミトコンドリアの発達と呼吸量の増加が一致することも明らかにされている[18]。

以前のわれわれの検討では，移植胚の選択は呼吸量評価のみで行うより，形態評価のみで行うほうが妊娠率は高くなることを示した（形態評価のみ39.3%，呼吸量評価のみ26.7%，2008年日本生殖医学会シンポジウムにて）。そこで今回は形態評価に呼吸量評価を加えることで，形態評価のみで選ぶよりも着床能を持った1個の胚を選択することができるか検討した。当院で移植時良好胚が2個以上存在する移植胚選別困難例での，Day 3時形態評価のみの胚盤胞到達率は9分割以上で67.1%，8分割は76.8%，7分割は59.3%，6分割は44.0%で8分割を示す胚で最も胚盤胞到達率が高かった。今回検討した9分割以上，7分割および6分割胚では呼吸量が大きくなるほど胚盤胞到達率は高くなる結果を示し，形態評価のみでも高率に胚盤胞へ発育する8分割では呼吸量の違いによる差は認めなかった。吉田[19]はDay 3に観察したとき，8分割を示す胚は他の分割を示す胚よりも，最も着床率が高くなることを報告しており，このことからもDay 3に良好な8分割を示していた胚はそれだけで十分高い発育能があることを示唆している。しかし，それ以外の胚では胚の呼吸量を測定することで，胚の品質を数値化して客観的に確認することができ，呼吸量の大きい

胚を選ぶことで，その後の発育可能な胚を見分けることが可能となる。

検討2のDay 3-eSETの検討では，前方視的検討として無作為に呼吸量を加えた群と形態評価のみで移植を行った群に振り分けたが，呼吸量を加えた群で妊娠率は高く，流産率も低くなり，それに伴い継続妊娠率が高くなる結果が得られた。形態評価がまったく等しく見える胚でもその後の発育能は異なり，このことが，呼吸量を測定することにより知りえたための結果であると考えられる。

呼吸量測定胚の出生結果でも呼吸量測定胚，非測定胚で差はみられないことが確認できた。

おわりに

胚の呼吸量を測定することは，形態評価のみでは知りえなかった胚の状態を数値化し，客観的に確認することができる。呼吸量測定を形態評価に加えることで，最も着床能のある1個の胚を選別することが可能となることが示された。

文　献

1) Mullin CM, Fino ME, Talebian S, et al : Comparison of pregnancy outcomes in elective single blastocyst transfer versus double blastocyst transfer stratified by age. Fertil Steril, **93** : 1837-1843, 2010. Epub Feb 27. 2009.
2) 那須　恵，後藤香里，熊迫陽子，他：電気化学的呼吸計測によるヒト胚のクオリティー評価．産婦の実際，**57** : 289-294, 2008.
3) Zollner U, Zollner KP, Hartl G, et al : The use of a detailed zygote score after IVF/ICSI to obtain good quality blastocysts : the German experience. Hum Reprod, **17** : 1327-1333, 2002.
4) Scott L, Alvero R, Leondires M, et al : The morphology of human pronuclear embryos is positively related to blastocyst development and implantation. Hum Reprod, **15** : 2394-2403, 2000.
5) Tesarik J, Greco E : The probability of abnormal preimplantation development can be predicted by a single static observation on pronuclear stage morphology. Hum Reprod, **14** : 1318-1323, 1999.
6) Ciray HN, Karaqenc L, Uluq U, et al : Early cleavage morphology affects the quality and implantation potential of day 3 embryos. Fertil Steril, **85** : 358-365, 2006
7) Gardner DK, Schoolcraft WB, Wargley L, et al : A prospective randomized trial of blastocyst culture and transfer in *in-vitro* fertilization. Fertil Steril, **13** : 3434-3440, 1998.
8) Coskun S, Hollanders J, Al-Hassan S, et al : Day 5 versus day 3 cmbryo transfer : a controlled randomized trial. Hum Reprod, **15** : 1947-1952, 2000.
9) Utsunomiya T, Ito H, Nagaki M, et al : A Prospective, Randomized Study : Day-3 versus Hatching Blastocyst Stage. Hum Reprod, **19** : 1598-1603, 2004.
10) Abe H, Matsuzaki S, Hoshi H : Ultrastructural differences in bovine morulae classified as high and low qualiies by morphological evaluation. Theriogenology, **57** : 1273-1283, 2002.
11) 阿部宏之：電気化学的イメージング技術を応用した胚のクオリティー評価．産婦の実際，**55** : 207-216, 2006.
12) Abe H, Shiku H, Aoyagi S, et al : *In vitro* culture and evaluation of embryos for production of high quality bovine embryos. J Mamm Ova Res, **21** : 22-30, 2004.
13) Shiku H, Shiraishi T, Ohya H, et al : Oxygen consumption of single bovine embryos probed with scanning electrochemical microscopy. Anal Chem. **73** : 3751-3758, 2001.
14) Shiku H, Shiraishi T, Aoyagi S, et al : Respiration activity of single bovine embryos entrapped in a cone-shaped microwell monitored by scanning electrochemical microscopy. Anal Chim Acta, **522** : 51-58, 2004.
15) Abe H, Shiku H, Yokoo M, et al : Evaluating the quality of individual embryos with a non-invasive and highly sensitive measurement of oxygen consumption by scanning electrochemical microscopy. J Reprod Dev, **52** (Suppl): S55-S64, 2006.
16) 後藤香里，小池　恵，熊迫陽子，他：電気化学的呼吸計測技術におけるヒト胚クオリティー評価と安全性．日受精着床会誌，**27** : 53-58, 2010.
17) Utsunomiya T, Goto K, Nasu M, et al : Evaluating the quality of human embryos with a measurement of oxygen consumption by scanning electrochemical microscopy. J Mamm Ova Res. **25** : 2-7, 2008.
18) 阿部宏之，横尾正樹，荒木康久，他：電気化学的イメージング法を応用した単一ヒト胚の呼吸能解析．産婦の実際，**56** : 2053-2057, 2007.
19) 吉田　淳：胚の選別と胚移植，ART実践マニュアル，p 63，永井書店，2005.

Influence of Tip Size on Single Yeast Cell Imaging Using Scanning Electrochemical Microscopy

*Kuniaki Nagamine, Yasufumi Takahashi, Kosuke Ino, Hitoshi Shiku, Tomokazu Matsue**

Graduate School of Environmental Studies, Tohoku University, 6-6-11, Aramaki-Aoba, Aoba, Sendai 980-8579, Japan
tel/fax: +81-22-795-7209
*e-mail: matsue@bioinfo.che.tohoku.ac.jp

Received: September 24, 2010
Accepted: January 10, 2011

Abstract
The influence of the tip reaction on the substrate generation/tip collection mode SECM imaging of a single yeast cell was investigated by using various sizes of probe electrodes in μm–nm scales because the tip reaction would disturb the concentration profile of intracellular enzyme reactant formed around the cell. GC mode measurements of a single yeast cell were performed using a dual mediator system with lipophilic menadione and hydrophilic ferricyanide. We found downscaling of the tip size enabled quantitative SECM imaging of a single cell in GC mode without disturbing the concentration profile of the mediator formed around the cell by the tip reaction.

Keywords: Scanning electrochemical microscopy, Nanoelectrodes, Single cell analysis

DOI: 10.1002/elan.201000595

1 Introduction

Quantitative analysis of intracellular enzyme activity in microbial cells including yeast cells has been required for investigation of cell physiology and cell-based diagnosis of pathologic conditions. In particular, measurement of cellular activity of a specific cell spatially localized in a densely packed cell population is helpful for revealing metabolic alteration in individual cells via cell-cell communication. This metabolic regulation is a requisite for microbial cells to survive in variable and cruel microenvironments and for some bacteria to induce pathogenic gene expression [1–4]. Therefore, development of single microbial cell analysis in a densely packed population has been expected to reveal the cell-cell communication in microbial cells and to improve the screening drugs used to inhibit pathogenic gene expression in an infectious cell.

Bioelectrochemical methods have provided the noninvasive quantitative analysis of intracellular redox enzyme activity using mediators that shuttle electrons between intracellular enzymes and the electrode placed extracellularly [5–10]. In addition, by means of scanning electrochemical microscopy (SECM), intracellular enzyme activity has been quantified in spatially localized single prokaryotic and eukaryotic cells [11–27]. In substrate generation/tip collection (GC) mode SECM, a concentration profile of intracellular enzyme reactant was detected by scanning a probe electrode above a target cell. Sensitivity of GC mode SECM is relatively high as the background signal is very low. However, when a probe electrode with a large active tip was used for GC mode imaging, the concentration profile of intracellular enzyme reactant formed around the cells might be disturbed by the consumption (or generation) of redox species at the tip itself. Downscaling of the tip size would suppress the disturbance of concentration profile and enables clear imaging of a single cell.

In this study, we investigated the influence of tip reaction on the GC mode SECM imaging of a single yeast cell by using various Pt electrode probes with tip sizes in μm–nm scales. The target intracellular enzyme was cytosolic and mitochondrial NAD(P)H-oxidizing enzymes (NOEs), which is the general term for all enzymes catalyzing electron transfer from NAD(P)H to quinone substrates. Figure 1 shows the principle of electrochemical detection of NOEs activity in the GC mode [5–10]. NOEs activity in a yeast cell was detected using a dual mediator system with lipophilic menadione and hydrophilic ferricyanide. Mauzeroll and Bard investigated the permeation of menadione through yeast cells, the intracellular formation of menadione-*S*-glutathione conjugate, and the efflux of the conjugate from the cells using GC mode SECM [28]. In this study, menadione shuttles electrons from intracellular NOEs to extracellular ferricyanide with low permeability to cell membrane, followed by ferrocyanide generation around the cell. SECM was used to monitor the ferrocyanide generation that reflects NOEs activity in yeast cell. We found that downscaling of the tip size enabled quantitative SECM imaging of a single yeast cell in GC mode without disturbing the concentration profile of mediator formed around the cell by the tip reaction.

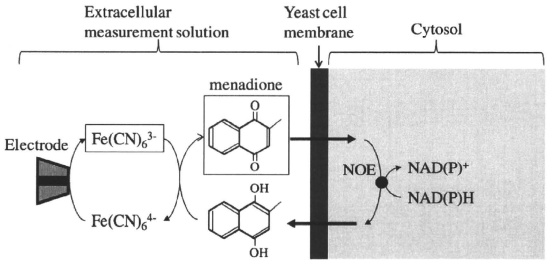

Fig. 1. Principle of electrochemical detection of NOEs activity in yeast cell. $Fe(CN)_6^{3-}$ and menadione (indicated by squares) were added to the measurement solution.

2 Experimental

2.1 Reagents

Potassium hexacyanoferrate(III), menadione, D-(+)-glucose were purchased from Wako Pure Chemicals Industries, Ltd. Ferrocene methanol ($FcCH_2OH$) was purchased from Sigma Aldrich. All solutions were prepared using distilled and deionized water from Direct-Q (Millipore).

2.2 Yeast Strain and Growth Conditions

Saccharomyces cerevisiae strain Y190 was donated by Dr. Fujio Shiraishi from the National Institute for Environmental Studies. The cells were cultured for 24 h at 30 °C with shaking at 100 rpm in modified SD medium (without tryptophan and leucine) [17]. The culture was collected as a pellet by centrifugation (6000 rpm for 5 min), washed twice with Z buffer (60.0 mM $Na_2HPO_4{\cdot}12H_2O$; 39.7 mM $NaH_2PO_4{\cdot}2H_2O$; 10.0 mM KCl; 10.0 mM $MgSO_4{\cdot}7H_2O$; pH 7.0), and then resuspended in Z buffer.

2.3 Fabrication of Pt Micro- and Nanoelectrodes

The fabrication of the Pt microelectrode was described previously [29]. A Pt nanoelectrode was fabricated by simultaneously pulling a quartz capillary and a Pt wire inserted into the capillary under vacuum using a CO_2 laser puller P-2000 (Sutter) [30–32]. First, an annealed Pt wire (25.0 μm diameter) was inserted into the middle of 100 mm long quartz capillary (1.0 mm outer diameter and 0.3 mm inner diameter). Then, the Pt wire was sealed into the quartz capillary by irradiating CO_2 laser to the middle of the capillary under the following parameters: heat = 960, filament = 4, velocity = 100, delay = 120 and pull = 0. The heating process was carried out for 30 s followed by a cooling time of 30 s. For tight sealing of the Pt wire into the capillary, the heating process was performed under reduced pressure by connecting each end of the quartz capillary to a vacuum line. The heating/cooling process was repeated 5 times to ensure a proper sealing. Later, the capillary was pulled under the following parameters to form two sets of Pt nanoelectrodes: heat = 885, filament = 2, velocity = 50, delay = 100, and pull = 100. A copper lead wire was inserted into the capillary to make an electrical connection with the Pt wire using a silver paste. Finally, the tip of the nanoelectrode was carefully polished using a diamond grinder (EG-6, Narishige) to expose the disk-shaped active surface of the Pt wire.

2.4 SECM Imaging of NOEs Activity in Bulk Yeast Cells

Yeast cells (4×10^4) were entrapped in a cylindrical-shaped poly(dimethylsiloxane) (PDMS) microwell (diameter, 450 μm; depth, 50 μm). The fabrication method of the PDMS microwell array has been described previously [17]. The suspension of yeast cells was dispersed on the PDMS microwell array and stabilized for 10 min until the cells were dropped into the wells. The excess yeast cells were removed by washing the surface of the PDMS microwell array with Z buffer two times. Finally, the measurement solution was poured on the PDMS microwell array for SECM measurements. The components of the measurement solution were as follows: 20 mM potassium hexacyanoferrate(III), 0.10 mM menadione, and 20 mM D-(+)-glucose in Z buffer.

Imaging experiments were carried out using a SECM system including an inverted microscope (TE300, Nikon), a current amplifier (Model 427, Keithley), a stepping motor-driven XY stage (Model D70, Suruga Seiki), and a piezoelectric motor-driven Z stage (E-501, Physik Instrumente). For positioning, the Pt probe microelectrode (Pt radius, 7.4 μm) was brought into contact with the substrate surface. From there the probe was vertically retracted 20.0 μm off the surface using the piezoelectric motor with a precision of 0.1 μm. The potential of the probe electrode was held at +0.60 V vs. Ag/AgCl to provide a steady-state oxidation current for reduced form of mediator. The electrode was vertically scanned from the

original set position to 1.0 mm away from the PDMS surface at a scan rate of 9.5 $\mu m\,s^{-1}$ to detect the ferrocyanide concentration profile formed around the microwell containing yeast cells.

2.5 SECM Imaging of NOEs Activity in Single or Several Yeast Cells

Single or groups of yeast cells were electrostatically immobilized on an aminosilanized glass (Matsunami Glass Ind. Ltd.). The suspension of yeast cells was dispersed on the glass substrate and stabilized for 10 min to allow attachment on the surface of the glass. Excess yeast cells were removed by washing the surface of the slide glass with Z buffer twice, followed by pouring the measurement solution on the slide glass. The measurement solution was Z buffer containing 20 mM potassium hexacyanoferrate(III), 0.10 mM menadione, and 20 mM D-(+)-glucose. The Pt probe micro- or nanoelectrode was positioned 7.0 μm above the substrate surface with a precision of 0.1 μm in vertical direction. The probe electrode was laterally scanned over yeast cells at a scan rate of 1.0 $\mu m\,s^{-1}$ to detect the concentration profile of ferrocyanide around the cells. The potential of the probe electrode was held at +0.60 V vs. Ag/AgCl to detect the oxidation current for ferrocyanide. The time required for SECM imaging at an area of $30\times30\ \mu m^2$ (spatial resolution, 1.0 μm) was approximately 30 min.

2.6 Quantitative Analysis of Mass Transfer Rate of Redox Mediator from Single Yeast Cell Using GC Mode SECM Imaging

Quantification of the mass transfer rate of the redox mediator from single yeast cell was carried out using GC mode SECM imaging as described previously [33]. When a spherically shaped cell is positioned on a flat substrate in a measurement solution, the mass transfer rate of the hemispherically diffusing redox mediator from the yeast cell (F_{yeast} in $mol\,s^{-1}$) in a steady-state rate can be estimated by multiplying the flux at a certain point ($f_{r=rx}$ in $mol\,cm^{-2}\,s^{-1}$, r refers to the distance from the cell surface) with the semi-spherical section area ($S_{r=rx}$ in cm^2)

$$F_{yeast} = f_{r=rx} \times S_{r=rx} \tag{1}$$

The $S_{r=rx}$ value is expressed as follows:

$$S_{r=rx} = 2\pi\, r_x^{\,2} \tag{2}$$

At $r=r_x$, the flux is expressed as

$$f_{r=rx} = D\,(\Delta C_{r=rx}/\Delta r) \tag{3}$$

Where D is the diffusion coefficient of a redox mediator (for ferrocyanide, $D_{ferro}=6.5\times10^{-6}\ cm^2\,s^{-1}$); $\Delta C_{r=rx}/\Delta r$ is the concentration gradient of the redox mediator, and $\Delta C_{r=rx}$ and Δr are expressed as

$$\Delta C_{r=rx} = |\ C_{r=rx} - C_{r=rx+\Delta r}\ | \tag{4}$$

$$\Delta r = |r_{r=rx} - r_{r=rx+\Delta r}\ | \tag{5}$$

The concentration gradient of a redox mediator at $r=r_x$ is calculated from the profiles of the redox current. The redox current observed with the SECM system is expressed by

$$I_{r=rx} = 4nFDC_{r=rx}\,a \tag{6}$$

Where n is the number of electrons per molecule reduced; F is the Faraday constant ($96\,500\ C\,mol^{-1}$); $C_{r=rx}$ is the local concentration of the redox mediator at $r=r_x$ ($mol\,cm^{-3}$); and a is the electrode radius (cm).

For SECM imaging using a dual mediator system, it was assumed that menadione is localized within the yeast cell and ferricyanide is outside of the cell. When the ferricyanide concentration is in large excess over the menadione concentration, menadione should not be detected directly with a SECM probe electrode because all the menadione is reoxidized by ferricyanide at the cell surface. If we assume that the concentration of menadione and ferricyanide is in large excess over the Michaelis constant value of NOEs and that the SECM probe detects the diffusion-limited current, the rate-limiting step for determining current response is the cellular reaction step including NOEs reaction rate and the permeation rate of mediator through the cell membrane [34].

3 Results and Discussion

Figure 2A shows the scanning electron micrograph (SEM) of the tip of the Pt nanoelectrode. The nanometer-sized Pt disk was clearly identified at the center of the insulating quartz sheath. At higher magnification, the radius of the Pt disk was determined to be approximately 300 nm (Figure 2B). Figure 2C shows a cyclic voltammogram (CV) of 0.50 mM $FcCH_2OH$ detected with the Pt nanoelectrode shown in Figure 2A. At the potential scan rate of 20 mV/s, CV showed a s-shaped curve with the steady-state current at +0.50 V vs. Ag/AgCl. Assuming the geometry of the nanoelectrode to be disk shaped, the steady-state current for a nanoelectrode in an insulating sheath is given by Equation 6 with the diffusion coefficient of $FcCH_2OH$ as $7.8\times10^{-6}\ cm^2\,s^{-1}$ [32] and the bulk concentration of $FcCH_2OH$ as $5.0\times10^{-7}\ mol\,cm^{-3}$. Using Equation 6, the radius of the nanoelectrode was calculated as 380 nm, which was almost the same size as the identified size from SEM observation.

Figure 3A shows the responses of 4×10^4 yeast cells entrapped in a PDMS microwell in 20 mM D-(+)-glucose solution containing (a) 20 mM ferricyanide, (b) 0.10 mM menadione, and (c) 20 mM ferricyanide and 0.10 mM menadione. The ordinate in Figure 3A represents the current change when the electrode set at +0.60 V vs. Ag/AgCl was vertically scanned from the original set position

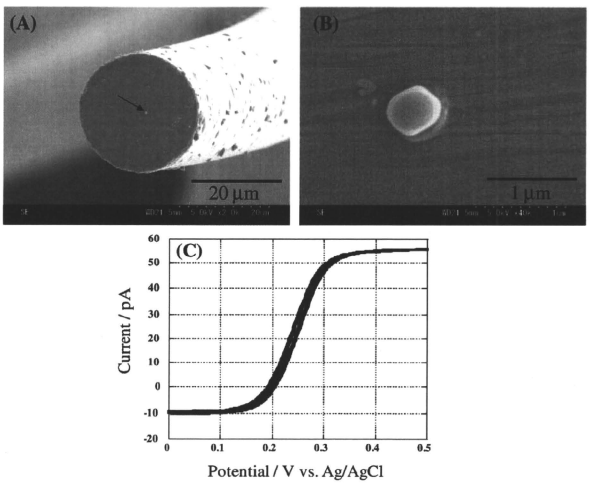

Fig. 2. A) Scanning electron micrograph of the tip of a Pt nanoelectrode. B) Pt disk of the same nanoelectrode as (A) at a higher magnification. C) Cyclic voltammogram of 0.50 mM $FcCH_2OH$ using the Pt nanoelectrode shown in (A). Scan rate: 20 $mV\,s^{-1}$.

(20.0 μm above the PDMS well surface) to 1.0 mm above from the well surface. When the solution contained only ferricyanide (Figure 3Aa), the current change was only several pA and almost no current variation was observed on scanning the electrode. This suggests almost no interaction of ferricyanide with the intracellular redox processes due to low permeability of hydrophilic ferricyanide through the yeast cell membrane. In the case of lipophilic menadione (Figure 3Ab), on the other hand, the current change became larger (48 pA). Menadione functions as a permeable redox mediator to interact with NOEs to form menadiol which diffuses into the solution to reduce ferricyanide to give oxidation current at the electrode probe (see Figure 1) [9]. In a dual mediator system (Figure 3Ac), the current change was 2.3 times higher than that with menadione alone in the solution. This tendency was in accordance with previous reports [5,6,9], which suggested that the enhancement of current change in the dual mediator system would attribute to the redox cycling reaction of menadione between ferricyanide and intracellular NOEs depicted in Figure 1 and the help of ferricyanide to overcome the slow heterogeneous redox kinetics of menadione on Pt electrodes [9].

For quantitative analysis of the mass transfer rate of the ferrocyanide from single yeast cell, we examined the concentration of the mediators in large excess over the Michaelis constant value of NOEs. Figure 3B shows the relationship between the mediator concentration and the current change in a dual mediator system. The current change was detected as described in Figure 3A. Each point in Figure 3B has relatively large error bar, because the differences in individual cellular activity caused variation of averaged activity of the cell population depending on the microenvironmental conditions. In Figure 3Ba, the current change tended to be saturated when the concentration of ferricyanide was higher than 1.0 mM in the presence of 0.10 mM menadione. When it was assumed that all of the 1.0 mM ferricyanide was reduced to ferrocyanide by menadiol and the ferrocyanide was oxidized at the 7.4 μm-radius tip in the bulk solution, the calculated oxidation current for ferrocyanide using the Equation 6 is 1.86 nA. This value is much larger than the current change for ferrocyanide generated from the cells in Figure 3Ac (48 pA) even when using 20 mM ferricyanide. These results suggested that more than 1.0 mM of ferricyanide concentration is in large excess over the Michaelis constant value of NOEs. In Figure 3Bb, the current changes increased with increase the menadione concentration and retarded at the concentration higher than 0.20 mM in the presence of 20 mM ferricyanide. Then, the current change gradually decreased when the cells were exposed to the solution containing more than 0.20 mM menadione. This behavior suggests the cytotoxicity of menadione or rapid exhaustion of NAD(P)H [9]. On the basis of these results, the concentrations of menadione and ferricyanide were set to 0.10 mM and 20 mM, respectively, for the dual mediator system.

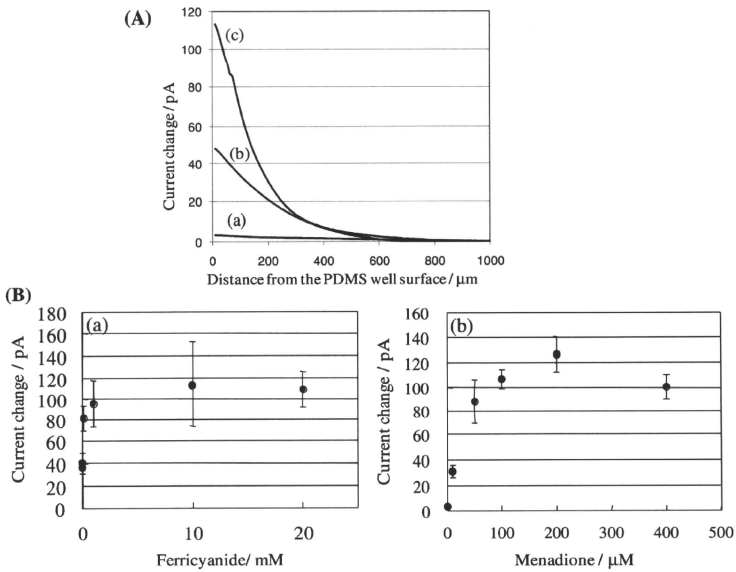

Fig. 3. A) Current changes when a Pt microelectrode probe retracted from 20 μm to 1.0 mm above from the PDMS microwell surface entrapped with 4×10^4 yeast cells in 20 mM D-(+)-glucose solution containing (a) 20 mM ferricyanide, (b) 0.10 mM menadione, and (c) 20 mM ferricyanide and 0.10 mM menadione. B) Current changes vs. concentration plots for (a) ferricyanide and (b) menadione. (a): Concentration of menadione was set at 0.10 mM. (b): Concentration of ferricyanide was set at 20 mM. Each point represents the mean of five measurements ± *SD*. Probe: Pt microelectrode with Pt radius of 7.4 μm. Potential of the probe: +0.60 V vs. Ag/AgCl.

Figure 4 shows the line scan responses for the dual mediator system of 4 aggregated yeast cells when a probe electrode with a Pt radius of (a) 11.9 μm, (b) 1.0 μm, or (c) 199 nm was scanned 7.0 μm above the surface of the glass substrate, together with the optical image of the cells. All the lines show peaks of oxidation current corresponding to the NOEs activity of yeast cells, although the change in the current from the baseline became small with decreasing tip size. The generation rate of ferrocyanide from a single yeast cell, F_{yeast}, was calculated based on Equation 1 and was found to be 3.07×10^{-19} (11.9-μm tip), 1.69×10^{-19} (1.0-μm tip), and 1.73×10^{-19} (199-nm tip) mol s^{-1} cell^{-1}. The generation rates detected using probes with 1.0 μm or 199 nm radii were almost identical and in good agreement with the value previously reported [5]. The oxidation rate for ferrocyanide at the probe electrode, F_{tip}, was calculated based on Equation 6 and found to be 8.05×10^{-20} (1.0-μm tip) and 1.73×10^{-20} (199-nm tip) mol s^{-1} at the peaks in Figure 4B. As F_{tip} at the 199-nm tip was sufficiently smaller than F_{yeast}, the ferrocyanide concentration profile around the cells would not be disturbed by the electrochemical reaction at the tip. However, each single cellular activity could not be resolved from the current response due to crossover of the ferrocyanide diffusion layers around the yeast cells. For the 11.9-μm tip, a large amount of ferrocyanide generated from a yeast cell would be consumed at the probe electrode ($F_{tip}=1.63\times10^{-18}$ mol s^{-1}). Therefore, local concentrations of ferrocyanide could not be precisely measured.

The signal-to-noise ratios in Figure 4B were 23.0 (signal = 668.1 fA, noise = 29.0 fA) for the 11.9-μm tip, 1.7 (signal = 29.0 fA, noise = 17.2 fA) for the 1.0-μm tip, 0.5 (signal = 14.3 fA, noise = 27.1 fA) for the 199-nm tip. Although the noise is in the range of the signal when using nanoelectrode, the increase of oxidation current for ferrocyanide was reproducibly detected around the yeast cells, suggesting the significant current response of the cells was detected using nanoelectrode.

The SECM measurements enabled the visualization of NOEs activity of an isolated single cell. Figure 5 shows the SECM image of a single yeast cell based on oxidation current for ferrocyanide in dual mediator system with the

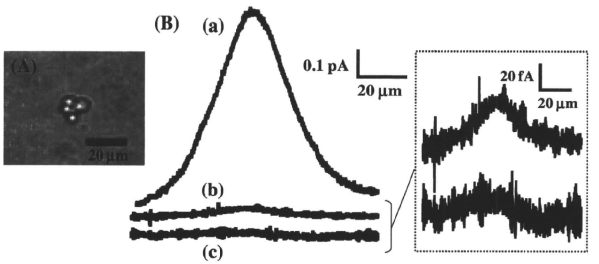

Fig. 4. A) The micrograph of 4 yeast cells. B) Current responses in line-scan images for 4 yeast cells in 20 mM D-(+)-glucose solution containing 20 mM ferricyanide and 0.10 mM menadione. Probe: Pt electrode with a Pt radius of (a) 11.9 μm, (b) 1.0 μm, and (c) 199 nm. Scan rate: 1.0 $\mu m\,s^{-1}$. Potential of the probe: +0.60 V vs.Ag/AgCl.

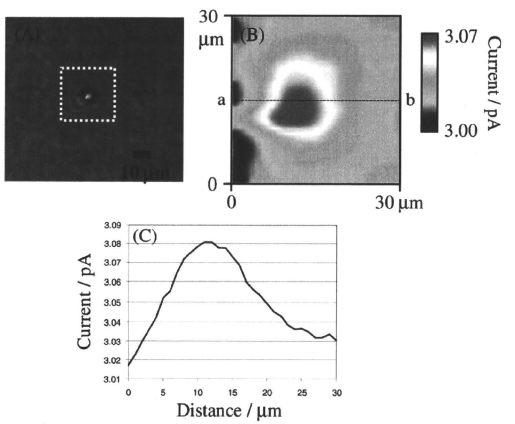

Fig. 5. A) Micrograph of a single yeast cell. B) SECM image of single yeast cell based on oxidation current for ferrocyanide in 20 mM D-(+)-glucose solution containing 20 mM ferricyanide and 0.10 mM menadione. C) Line scan along the cross section a–b in (B). Probe: Pt nanoelectrode with the Pt radius of 450 nm. Potential of the probe: +0.60 V vs. Ag/AgCl. Scan rate: 1.0 $\mu m\,s^{-1}$.

electrode probe of 450 nm-tip, together with an optical image of the cell. The enhanced current around the cell clearly indicated the NOEs activity of the yeast cell in Figure 5B. Figure 5C shows the line scan along the cross section a-b in Figure 5B. The signal-to-noise ratio calculated from the line scan was 7.7 (signal = 63.7 fA, noise = 8.24 fA), suggesting a significant response of the single yeast cell. Half-width of the current profile for ferrocyanide was found to be 14 μm, which was significantly larger than the size of yeast cell (5.0 μm in diameter). It should be noted again that, regardless of tip diameter, single-cell level resolution in cell aggregates is difficult in the present constant-height GC mode SECM imaging due to spread of the ferrocyanide diffusion layer around the cell.

4 Conclusions

Influence of tip reaction on the GC mode SECM imaging of a single yeast cell was investigated by using various Pt electrode probes with tip sizes in μm–nm scales. The quantitative imaging of NOEs activity in an isolated yeast cells was successfully achieved in the GC mode measurements using the 199 nm-tip without disturbing the mediator concentration profile formed around the cells by the

tip reaction. However, spatial resolution of the SECM image was not improved even when the tip size was downscaled due to spread of the ferrocyanide diffusion layer around the cell. To obtain higher resolution of single cellular images in GC mode, one has to incorporate an accurate cell-benign distance control mechanism at nanometer scale into the SECM system. We think a shear-force or an ion-conductance feedback control is the probable candidate for the distance control. Using these distance control mechanisms, topographic and electrochemical images of locally immobilized cells were captured simultaneously in nanometer-order resolution using standing approach mode SECM [19–22]. In the future, the SECM system with a cell-benign distance control will be applied for characterization of single live yeast cells in a densely-packed population.

Acknowledgements

This work was partly supported by Grants-in-Aid for Scientific Research (18101006, 9750055, 22245011) from *MEXT (Ministry of Education, Culture, Sports, Science and Technology)*, Japan and by a grant from the *Center for Interdisciplinary Research, Tohoku University.* K. N. acknowledges *G-COE*.

References

[1] M. A. Aon, S. Cortassa, K. M. Lemar, A. J. Hayes, D. Lloyd, *FEBS Lett.* **2007**, *581*, 8.
[2] D. B. Murray, M. Beckmann, H. Kitano, *Proc. Natl. Acad. Sci. USA* **2007**, *104*, 2241.
[3] Z. Palkova, L. Vachova, *FEMS Microbiol. Rev.* **2006**, *30*, 806.
[4] C. T. Parker, V. Sperandlo, *Cell. Microbiol.* **2009**, *11*, 363.
[5] K. H. R. Baronian, A. J. Downard, R. K. Lowen, *Appl. Micribiol. Biotechnol.* **2002**, *60*, 108.
[6] A. Heiskanen, J. Yakovleva, C. Spegel, R. Taboryski, M. Koudelka-Hep, J. Emneus, T. Ruzgas, *Electrochem. Commun.* **2004**, *6*, 219.
[7] A. Heiskanen, C. Spegel, N. Kostesha, S. Lindahl, T. Ruzgas, J. Emneus, *Anal. Biochem.* **2009**, *384*, 11.
[8] J. D. Rabinowitz, J. F. Vacchino, C. Beeson, H. M. McConnel, *J. Am. Chem. Soc.* **1998**, *120*, 2464.
[9] C. F. Spegel, A. R. Heiskanen, N. Kostesha, T. H. Johanson, M. F. G. Grauslund, M. Koudelka-Hep, J. Emnus, T. Ruzgas, *Anal. Chem.* **2007**, *79*, 8919.
[10] J. Zhao, M. Wang, Z. Yang, Z. Wang, H. Wang, Z. Yang, *Anal. Chim. Acta* **2007**, *597*, 67.
[11] C. Amatore, S. Arbault, M. Erard, *Anal. Chem.* **2008**, *80*, 9635.
[12] C. Cai, B. Liu, M. V. Mirkin, H. A. Frank, J. F. Rusling, *Anal. Chem.* **2002**, *74*, 114.
[13] W. Feng, S. A. Rotenberg, M. V. Mirkin, *Anal. Chem.* **2003**, *75*, 4148.
[14] D. T. Pierce, A. J. Bard, *Anal. Chem.* **1993**, *65*, 3598.
[15] H. Shiku, T. Shiraishi, H. Ohya, T. Matsue, H. Abe, H. Hoshi, M. Kobayashi, *Anal. Chem.* **2001**, *73*, 3751.
[16] H. Shiku, T. Shiraishi, S. Aoyagi, Y. Utsumi, M. Matsudaira, H. Abe, H. Hoshi, S. Kasai, H. Ohya, T. Matsue, *Anal. Chim. Acta* **2004**, *522*, 51.
[17] H. Shiku, S. Goto, S. Jung, K. Nagamine, M. Koide, T. Itayama, T. Yasukawa, T. Matsue, *Analyst* **2009**, *134*, 182.
[18] P. Sun, F. O. Laforge, T. P. Abeyweera, S. A. Rotenberg, J. Carpino, M. V. Mirkin, *Proc. Natl. Acad. Sci. USA* **2008**, *105*, 443.
[19] Y. Takahashi, Y. Hirano, T. Yasukawa, H. Shiku, H. Yamada, T. Matsue, *Langmuir* **2006**, *22*, 10299.
[20] Y. Takahashi, T. Miyamoto, H. Shiku, R. Asano, T. Yasukawa, I. Kumagai, T. Matsue, *Anal. Chem.* **2009**, *81*, 2785.
[21] Y. Takahashi, H. Shiku, T. Murata, T. Yasukawa, T. Matsue, *Anal. Chem.* **2009**, *81*, 9674.
[22] Y. Takahashi, A. I. Shevchuk, P. Novak, Y. Murakami, H. Shiku, Y. E. Korchev, T. Matsue, *J. Am. Chem. Soc.* **2010**, *132*, 10118.
[23] T. Yasukawa, Y. Kondo, I. Uchida, T. Matsue, *Chem. Lett.* **1998**, *8*, 767.
[24] T. Yasukawa, I. Uchida, T. Matsue, *Biochim. Biophys. Acta, Biomemb.* **1998**, *1369*, 152.
[25] T. Yasukawa, I. Uchida, T. Matsue, *Biophys. J.* **1999**, *76*, 1129.
[26] L. Zhu, N. Gao, X. Zhan, W. Jin, *Talanta* **2008**, *77*, 804.
[27] R. Zhu, S. M. Macfie, Z. Ding, *Anal. Chem.* **2008**, *24*, 14261.
[28] J. Mauzeroll, A. J. Bard, *Proc. Natl. Acad. Sci. USA* **2004**, *101*, 7862.
[29] T. Matsue, S. Koike, T. Abe, T. Itabashi, I. Uchida, *Biochim. Biophys. Acta* **1992**, *1101*, 69.
[30] B. B. Katemann, W. Schuhmann, *Electroanalysis* **2002**, *14*, 22.
[31] Y. Shao, M. V. Mirlin, G. Fish, S. Kokotov, D. Palanker, A. Lewis, *Anal. Chem.* **1997**, *69*, 1627.
[32] P. Sun, M. V. Mirkin, *Anal. Chem.* **2006**, *78*, 6526.
[33] T. Kaya, D. Numai, K. Nagamine, S. Aoyagi, H. Shiku, T. Matsue, *Analyst* **2004**, *129*, 529.
[34] K. Nagamine, T. Kaya, T. Yasukawa, H. Shiku, T. Matsue, *Sens. Actuators B* **2005**, *108*, 676.

J|A|C|S
ARTICLES

Published on Web 06/30/2010

Simultaneous Noncontact Topography and Electrochemical Imaging by SECM/SICM Featuring Ion Current Feedback Regulation

Yasufumi Takahashi,[†] Andrew I. Shevchuk,[‡] Pavel Novak,[‡] Yumi Murakami,[†] Hitoshi Shiku,[†] Yuri E. Korchev,*[,‡] and Tomokazu Matsue*[,†]

Graduate School of Environmental Studies, Tohoku University, Aramaki Aoba 6-6-11-605, Sendai 980-8579, Japan, and Division of Medicine, Imperial College London, Hammersmith Hospital Campus, London W12 0NN, United Kingdom

Received April 9, 2010; E-mail: matsue@bioinfo.che.tohoku.ac.jp

Abstract: We described a hybrid system of scanning electrochemical microscopy (SECM) and scanning ion conductance microscopy (SICM) with ion current feedback nanopositioning control for simultaneous imaging of noncontact topography and spatial distribution of electrochemical species. A nanopipette/nanoring electrode probe provided submicrometer resolution of the electrochemical measurement on surfaces with complex topology. The SECM/SICM probe had an aperture radius of 220 nm. The inner and outer radii of the SECM Au nanoring electrode were 330 and 550 nm, respectively. Characterization of the probe was performed with scanning electron microscopy (SEM), cyclic voltammetry (CV), and approach curve measurements. SECM/SICM was applied to simultaneous imaging of topography and electrochemical responses of enzymes (horse radish peroxidase (HRP) and glucose oxidase (GOD)) and single live cells (A6 cells, superior cervical ganglion (SCG) cells, and cardiac myocytes). The measurements revealed the distribution of activity of the enzyme spots on uneven surfaces with submicrometer resolution. SECM/SICM acquired high resolution topographic images of cells together with the map of electrochemical signals. This combined technique was also applied to the evaluation of the permeation property of electroactive species through cellular membranes.

Introduction

A high temporal and spatial resolution analytical tool working in physiological conditions is needed to evaluate the relationship of the localized topography and function of biomolecules. Scanning electrochemical microscopy (SECM) uses a micro- or nanoelectrode as a scanning probe and provides sample surface electrochemical property under physiological conditions without physical contact. SECM has been applied for evaluating the enzyme[1−6] and cellular activity,[7,8] estimating cell membrane permeability,[9−18] and detecting electroactive metabolic chemicals with short life spans, such as neurotransmitters[19,20] and nitric oxide (NO)[21] in the vicinity of living cellular surfaces. Membrane protein has also been detected with SECM.[22] Miniaturization of the probe electrode is important for improving the temporal and spatial resolution. In addition, a fine distance regulation system is required to approach the probe electrode against live cell surfaces.

† Tohoku University.
‡ Imperial College London.

(1) Wittstock, G. *Fresenius J. Anal. Chem.* **2001**, *370*, 303–315.
(2) Luo, H. Q.; Shiku, H.; Kumagai, A.; Takahashi, Y.; Yasukawa, T.; Matsue, T. *Electrochem. Commun.* **2007**, *9*, 2703–2708.
(3) Lei, R.; Stratmann, L.; Schafer, D.; Erichsen, T.; Neugebauer, S.; Li, N.; Schuhmann, W. *Anal. Chem.* **2009**, *81*, 5070–5074.
(4) Schafer, D.; Maciejewska, M.; Schuhmann, W. *Biosens. Bioelectron.* **2007**, *22*, 1887–1895.
(5) Maciejewska, M.; Schafer, D.; Schuhmann, W. *Electroanalysis* **2006**, *18*, 1916–1928.
(6) Hussien, E. M.; Erichsen, T.; Schuhmann, W.; Maciejewska, M. *Anal. Bioanal. Chem.* **2008**, *391*, 1773–1782.
(7) Li, X.; Bard, A. J. *J. Electroanal. Chem.* **2009**, *628*, 35–42.
(8) Takahashi, Y.; Hirano, Y.; Yasukawa, T.; Shiku, H.; Yamada, H.; Matsue, T. *Langmuir* **2006**, *22*, 10299–10306.
(9) Yasukawa, T.; Uchida, I.; Matsue, T. *Biochim. Biophys. Acta Biomembr.* **1998**, *1369*, 152–158.
(10) Barker, A. L.; Macpherson, J. V.; Slevin, C. J.; Unwin, P. R. *J. Phys. Chem. B* **1998**, *102*, 1586–1598.
(11) Gonsalves, M.; Barker, A. L.; Macpherson, J. V.; Unwin, P. R.; O'Hare, D.; Winlove, C. P. *Biophys. J.* **2000**, *78*, 1578–1588.
(12) Cannan, S.; Zhang, J.; Grunfeld, F.; Unwin, P. R. *Langmuir* **2004**, *20*, 701–707.
(13) Liu, B.; Rotenberg, S. A.; Mirkin, M. V. *Proc. Natl. Acad. Sci. U.S.A.* **2000**, *97*, 9855–9860.
(14) Liu, B.; Cheng, W.; Rotenberg, S. A.; Mirkin, M. V. *J. Electroanal. Chem.* **2001**, *500*, 590–597.
(15) Cai, C.; Liu, B.; Mirkin, M. V.; Frank, H. A.; Rusling, J. F. *Anal. Chem.* **2002**, *74*, 114–119.
(16) Liu, B.; Rotenberg, S. A.; Mirkin, M. V. *Anal. Chem.* **2002**, *74*, 6340–6348.
(17) Feng, W.; Rotenberg, S. A.; Mirkin, M. V. *Anal. Chem.* **2003**, *75*, 4148–4154.
(18) Sun, P.; Laforge, F. O.; Abeyweera, T. P.; Rotenberg, S. A.; Carpino, J.; Mirkin, M. V. *Proc. Natl. Acad. Sci. U.S.A.* **2008**, *105*, 443–448.
(19) Hengstenberg, A.; Blochl, A.; Dietzel, I. D.; Schuhmann, W. *Angew. Chem., Int. Ed.* **2001**, *40*, 905–908.
(20) Kurulugama, R. T.; Wipf, D. O.; Takacs, S. A.; Pongmayteegul, S.; Garris, P. A.; Baur, J. E. *Anal. Chem.* **2005**, *77*, 1111–1117.
(21) Isik, S.; Schuhmann, W. *Angew. Chem., Int. Ed.* **2006**, *45*, 7451–7454.
(22) Takahashi, Y.; Miyamoto, T.; Shiku, H.; Asano, R.; Yasukawa, T.; Kumagai, I.; Matsue, T. *Anal. Chem.* **2009**, *81*, 2785–2790.

10.1021/ja1029478

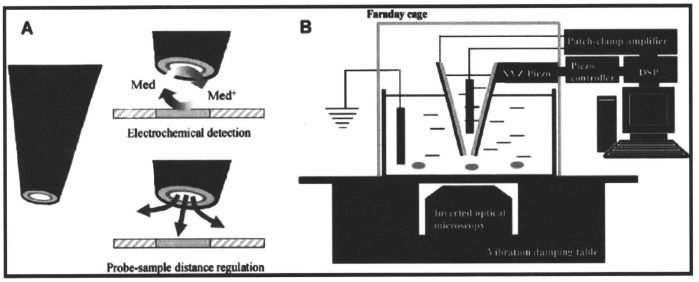

Figure 1. (A) Schematic illustration of the SECM/SICM system probe and (B) the SECM/SICM setup.

Significant efforts have been made to bring the electrode proximate with the sample surface using AFM,[23−26] shear force,[8,19,27] and impedance.[20] An electrode-patterned cantilever for the AFM/SECM system was fabricated and applied to simultaneous measurements. Carbon nanotube,[24] high resistive polymer,[25] and nanofabrication technique[26] have been adapted for making high aspect ratio shape probes. Nevertheless, it was difficult to apply the system to the measurement of soft samples because the force interaction was usually very unstable to serve as a feedback signal. The degradation of the electrochemical sensitivity caused by undesired electrochemical reactions at the side surfaces of the cantilever is also a problem. Shear force feedback regulation has also been used for control of the probe electrode sample distance. Previously, we reported the simultaneous imaging of the topography and electrochemical signals of single living cells using shear force distance regulation of a ring-type nanoelectrode probe.[27] However, preventing probe−cell contact was still difficult because the solution viscosity interfered with the shear force detection. Impedance-based probe−sample distance regulation has been used as a feedback mechanism for noncontact living cell imaging; however, it is difficult to improve the resolution of topography imaging because miniaturization of the electrode degrades the resistance signals for regulating the probe−sample distance.

Scanning ion conductance microscopy (SICM) uses a nanopipette as a scanning probe and provides living cell surface topography images under physiological conditions without physical contact.[28] Recent advances in SICM resulted in the development of a novel hopping probe ion conductance microscopy (HPICM) that allows topographical imaging of most convoluted surfaces.[29] SICM is based on the phenomenon that the ion flow through a sharp fluid-filled nanopipette is partially occluded when the nanopipette approaches the surface of a sample. Living cell surface topography and dynamic measurements have been performed. Topographical information of the live cell surface can be used to improve the resolution of other analytical tools; SICM nanopositioning system was combined with near field scanning optical microscopy,[30] confocal microscopy,[31] and patch clamps.[32,33] The nanopipette not only can detect localized ions but can also provide specific ion and biomolecules in a localized place.[34]

Hersam and co-workers reported combining SECM and SICM and demonstrated simultaneous submicrometer resolution topography and electrochemical imaging of gold film electrodes.[35] They used atomic layer deposition (ALD) of aluminum oxide to conformally insulate a gold-coated nanopipette and focused ion beam (FIB) milling to precisely expose the electrode surface. Bard et al. reported a similar probe design to dispense small amounts of a solution while monitoring the electrochemical response.[36]

In this work, we demonstrate a hybrid system of SECM and HPICM for simultaneous imaging of topography and electrochemical signal. This system is particularly suitable for detailed characterization of soft biomaterials with complex 3D structures, such as live cells. Figure 1 shows the structure of a nanopipette/nanoring electrode probe and a schematic diagram of the SECM/SICM measurement setup. Ion current flowing between Ag/AgCl electrodes located inside the nanopipette and the outside solution was used as the feedback signal for distance control. The electrochemical signal was acquired with the nanoring electrode. The present study demonstrates that the SECM/SICM system can generate submicrometer resolution images based on topography and electrochemical signals of enzymes on solid surfaces and convoluted living cells. The system was also found to be applicable

(23) Macpherson, J. V.; Unwin, P. R.; Hillier, A. C.; Bard, A. J. *J. Am. Chem. Soc.* **1996**, *118*, 6445–6452.
(24) Burt, D. P.; Wilson, N. R.; Weaver, J. M. R.; Dobson, P. S.; Macpherson, J. V. *Nano Lett.* **2005**, *5*, 639–643.
(25) Patil, A.; Sippel, J.; Martin, G. W.; Rinzler, A. G. *Nano Lett.* **2004**, *4*, 303–308.
(26) Shin, H.; Hesketh, P. J.; Mizaikoff, B.; Kranz, C. *Anal. Chem.* **2007**, *79*, 4769–4777.
(27) Takahashi, Y.; Shiku, H.; Murata, T.; Yasukawa, T.; Matsue, T. *Anal. Chem.* **2009**, *81*, 9674–9681.
(28) Korchev, Y. E.; Bashford, C. L.; Milovanovic, M.; Vodyanoy, I.; Lab, M. J. *Biophys. J.* **1997**, *73*, 653–658.
(29) Novak, P.; Li, C.; Shevchuk, A. I.; Stepanyan, R.; Caldwell, M.; Hughes, S.; Smart, T. G.; Gorelik, J.; Ostanin, V. P.; Lab, M. J.; Moss, G. W.; Frolenkov, G. I.; Klenerman, D.; Korchev, Y. E. *Nat. Methods* **2009**, *6*, 279–281.
(30) Korchev, Y. E.; Raval, M.; Lab, M. J.; Gorelik, J.; Edwards, C. R. W.; Rayment, T.; Klenerman, D. *Biophys. J.* **2000**, *78*, 2675–2679.
(31) Gorelik, J.; Shevchuk, A.; Ramalho, M.; Elliott, M.; Lei, C.; Higgins, C. F.; Lab, M. J.; Klenerman, D.; Krauzewicz, N.; Korchev, Y. *Proc. Natl. Acad. Sci. U.S.A.* **2002**, *99*, 16018–16023.
(32) Korchev, Y. E.; Negulyaev, Y. A.; Edwards, C. R. W.; Vodyanoy, I.; Lab, M. J. *Nat. Cell Biol.* **2000**, *2*, 616–619.
(33) Gorelik, J.; Gu, Y. C.; Spohr, H. A.; Shevchuk, A. I.; Lab, M. J.; Harding, S. E.; Edwards, C. R. W.; Whitaker, M.; Moss, G. W. J.; Benton, D. C. H.; Sanchez, D.; Darszon, A.; Vodyanoy, I.; Klenerman, D.; Korchev, Y. E. *Biophys. J.* **2002**, *83*, 3296–3303.
(34) Piper, J. D.; Li, C.; Lo, C. J.; Berry, R.; Korchev, Y.; Ying, L. M.; Klenerman, D. *J. Am. Chem. Soc.* **2008**, *130*, 10386–10393.
(35) Comstock, D. J.; Elam, J. W.; Pellin, M. J.; Hersam, M. C. *Anal. Chem.* **2010**, *82*, 1270–1276.
(36) Walsh, D. A.; Fernandez, J. L.; Mauzeroll, J.; Bard, A. *J. Anal. Chem.* **2005**, *77*, 5182–5188.

for evaluating the permeation property of electroactive species through cellular membranes. To our knowledge, this is the first report of high-resolution imaging of biomaterials with SECM/SICM.

Material and Methods

Reagents. Glucose oxidase (GOD; Biozyme Laboratories), horse radish peroxidase (HRP; Wako), L-15 medium (Gibco, Parsley, UK), ferrocenylmethanol ($FcCH_2OH$; Aldrich), potassium hexacyanoferrate (II) trihydrate ($K_4Fe(CN)_6 \cdot 3H_2O$; Kanto chemical Co., Inc.), glutaraldehyde (GA; Wako), and bovine serum albumin (BSA; Wako) were purchased and used as received. PBS was prepared from 7.2 mM Na_2HPO_4 $12H_2O$, 2.8 mM KH_2PO_4, and 150 mM NaCl (pH 7.0).

Fabrication of the SECM/SICM Electrode. A glass capillary (World precision Instruments, Inc., PG10165-4) was pulled using a capillary puller (Narishige PE-21). This capillary was then coated by Ti/Pt or Ti/Au sputtering (Anelva, L-332S-FH, RF200), followed by insulation with an anodic electrophoretic paint (Elecoat AE-X, Shimizu Co., Ltd.) by immersing the top of the metal-coated capillary and applying a DC potential of +2.0 V for 2 min between the capillary and counter electrode. After electrophoretic deposition, the electrode was removed from the solution, washed for 10 s to remove excess paint solution, and cured in an oven for 45 min at 150 °C to harden the insulation layer. To expose an electroactive area and form an ion transport aperture, the probe apex was milled by a focused ion beam (FIB, Seiko Instruments, SMI 2050).

Preparation of the Enzyme Spot. A PBS solution containing 1 mg/mL enzyme, 5 mg/mL BSA, and 1% GA was spotted on an APS-coated glass slide (Matsunami Glass Ind., Ltd.) and dried in air for 30 min.

Cell Culture and Isolation. A single A6 cell line was kindly provided by Dr. P. DeSmet (Karnolieke Universiteit, Belgium). All experiments were performed between 127 and 134 passages. Cells were cultured, as described previously.[37]

Superior cervical ganglion (SCG) cells were kindly provided by Dr. Guy Moss. Cells were cultured at a high density (9×10^5 cells/mL) on poly-L-lysine-coated coverslips. Cells were kept in a growth medium consisting of a DMEM (Gibco) supplemented with 10% fetal bovine serum (Gibco), 100 μg/mL streptomycin and 100 U/mL penicillin (Gibco), nerve growth factor (67 ng/mL, 2.5 S; Gibco). Cells were maintained at 37 °C in an atmosphere of humidified air with 95% O_2/5% CO_2. Cells were used for SECM/SICM measurements after 2−5 days when they had migrated to form cell clusters connected by axon bundles.

Cardiac myocytes from adult rats were isolated by digestion of intact perfused ventricle, according to the method previously described.[38]

Instrumentation. Figure 1B shows a schematic diagram of the SECM/SICM instrument, which has been previously described.[32] The currents were measured with a dual channel MultiClamp700B patch-clamp amplifier (Axon Instruments). The electrochemical and ion current signals were low-pass filtered at 40 Hz and 1 kHz, respectively. The data was digitized and analyzed with continuous data acquisition hardware and software (Axon Digidata 1322A, Axon Instruments). The probe position was controlled by a *XY* and *Z* piezoelectric scanner (Physik Instrumente, 621.2CL and 621.ZCL), which was controlled with an amplifier module (Physik Instrumente, E-503.00) and servo control module (Physik Instrumente, E-509.C3). The system was controlled by a program written with Delphi (Borland) and Code Composer Studio (Texas Instruments, U.S.A.) for ScanIC controller (Ionscope, UK).

SECM/SICM Measurements. The nanopipette electrode brought near the sample surface used ion current as the feedback signal and acquired height information. The electrochemical measurement was performed by the nanoring electrode. A hopping mode[29] was adopted as the scanning method. Briefly, the vertical *Z* positioning of the hopping probe and the movement of the sample in the *XY* plane were controlled at a sampling frequency of 20 kHz. A five-step procedure was used to determine the height and detect electrochemical species of the specimen at each imaging point. First, the probe was withdrawn a specified distance from its existing position. Second, the vertical position of the probe was maintained for 10 ms, while the nanopositioning stage moved to a new imaging point in the *XY* plane. During this time a reference current, I_{REF}, was measured as an average of the DC current through the probe. Third, the probe was lowered at constant fall rate of 15 nm/ms while monitoring the difference in the current, I, between I_{REF} and the instantaneous current through the probe I_{MV}. As soon as I drop exceeded the specified value of the set point, I_S, which was approximately 1.0−1.5% of I_{REF}, the vertical position of the probe was saved into the corresponding image pixel. Fourth, electrochemical measurement was performed for 200 μs using the nanoring electrode. Finally, the probe was quickly withdrawn by a specified hop amplitude to start a new measurement cycle.

Results and Discussion

Characterization of the SECM/SICM Probe. Panels A and B of Figure 2 show the SEM images and the structure of the SECM/SICM probe apex, respectively. The nanopipette aperture radius was found to be 220 nm. The Au nanoring electrode for SECM measurements was fabricated outside of the glass sheath, and the inner and outer radii of the nanoring electrode were found to be 330 and 550 nm, respectively. The SECM nanoring electrode was coated with a 70 nm thick insulator film. The probe angle was less than 10°, which allowed the probe to access a relatively high aspect sample. Figure 2C shows a cyclic voltammogram (CV) of 0.50 mM ferrocenylmethanol ($FcCH_2OH$), observed on the SECM nanoring electrode in 0.1 M KCl at a scanning rate of 100 mV/s. The voltammogram shows a sigmoidal shape with the steady-state current of 500 pA, which is approximately 6 times larger than that expected for a microdisk electrode with the same electrode size. The larger current is probably due to defects in the insulating layer. The defects did not cause a serious problem in SECM imaging based on generation collection (GC) and feedback (FB) measurements, as shown later. The SECM/SICM probe with a SECM Pt nanoring electrode also showed similar electrochemical behavior. Since the Pt nanoring electrode showed undesirable electrochemical responses in H_2O_2 solution, the probe with an Au nanoring electrode was used for imaging in H_2O_2 solutions, as described later.

Figure 3 shows approach curves to conductive and insulating substrates. The potentials of the SECM Pt and SICM Ag/AgCl electrodes were set at 500 and 200 mV, respectively. In either case, the ion current signal decreased as the tip approached the sample surface ($z \rightarrow 0$), which illustrates the fundamental nature of the ion current, blocked by either electron-insulating or electron-conducting surfaces. The distance for a 1% change of the SICM response (ion current) was almost the same as the nanopipette inner radius, in this case 220 nm. The experimental results were in good agreement with theory classified in reference 28, On the other hand, the approach curves of the electrochemical current signal for the insulating and conducting substrates showed negative and positive feedback features, respectively. The change in the electrochemical current was small probably due to the electrochemical reaction through the defects of the probe insulating wall. Importantly, no interference

(37) Gorelik, J.; Shevchuk, A. I.; Frolenkov, G. I.; Diakonov, I. A.; Lab, M. J.; Kros, C. J.; Richardson, G. P.; Vodyanoy, I.; Edwards, C. R. W.; Klenerman, D.; Korchev, Y. E. *Proc. Natl. Acad. Sci. U.S.A.* **2003**, *100*, 5819–5822.

(38) Lyon, A. R.; MacLeod, K. T.; Zhang, Y.; Garcia, E.; Kanda, G. K.; Lab, M. J.; Korchev, Y. E.; Harding, S. E.; Gorelik, J. *Proc. Natl. Acad. Sci. U.S.A.* **2009**, *106*, 6854–6859.

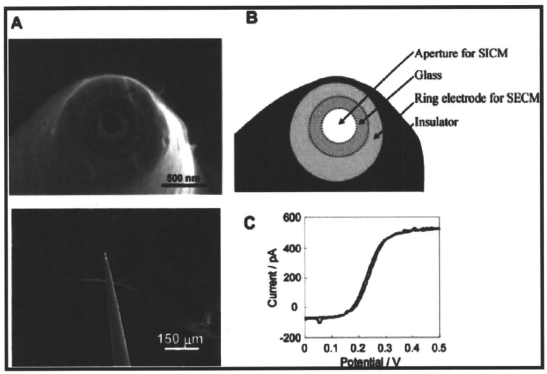

Figure 2. (A) SEM micrographs of the SECM/SICM probe. (B) Schematic illustration of probe structure. (C) Cyclic voltammogram of 0.50 mM $FcCH_2OH$ on a SECM nanoring electrode in a 0.1 M KCl solution at a scanning rate of 100 mV/s. The nanopipette aperture radius was 220 nm. Inner and outer radii of the SECM Au nanoring electrode were 330 and 550 nm, respectively. The insulator was 70 nm thick.

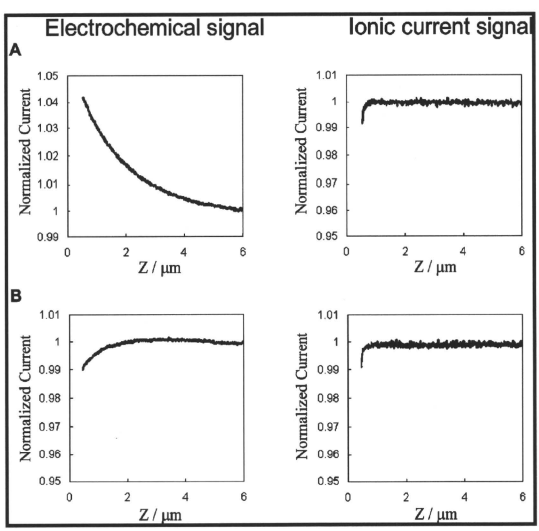

Figure 3. Approach curves of a SECM/SICM electrode to a (A) conductive Pt and (B) insulated glass surface in a 0.50 mM $FcCH_2OH$ + 0.1 M KCl solution for simultaneous electrochemical (left) and ion current (right) measurements. The SECM nanoring and SICM nanopipette electrodes were held at 500 and 300 mV vs Ag/AgCl, respectively.

was observed from CV measurements between the ion and electrochemical currents at the electrodes (Supporting Information, Figure S1). This indicated that interference between the nanoring electrode and Ag/AgCl electrode does not occur in simultaneous topographical and electrochemical imaging.

Imaging a Pt Interdigitated Array Electrode (IDA). We measured a Pt interdigitated array electrode (IDA) to show the noncontact distance regulation of SECM/SICM. If the probe collides with the IDA during scanning, it may break, resulting in an abrupt ion current increase, making it impossible to

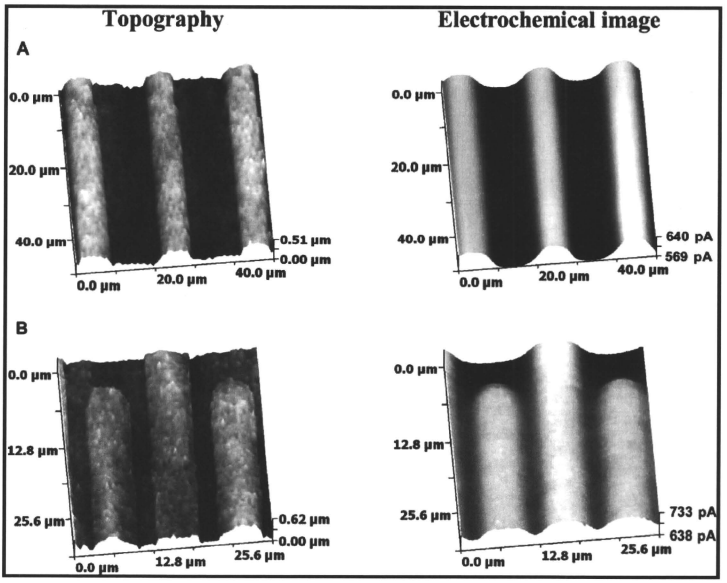

Figure 4. Topographic (left) and electrochemical (right) images of a Pt band microarray in 0.50 mM $FcCH_2OH$ + 0.1 M KCl. The SECM nanoring and SICM nanopipette electrodes were held at 500 and 300 mV vs Ag/AgCl, respectively. Scan ranges were (A) 50 μm × 50 μm and (B) 32 μm × 32 μm.

maintain constant distance regulation. Furthermore, the SECM electrochemical current increases if the nanoring electrode contacts and forms a short circuit with the Pt IDA. Figure 4 shows the SECM/SICM images of the Pt IDA in a solution containing 0.50 mM $FcCH_2OH$ and 0.1 M KCl. The potentials of the SECM Pt nanoring and SICM Ag/AgCl electrodes were 500 and 200 mV, respectively. When the probe moved above the Pt IDA, the electrochemical signal increased due to positive feedback resulting from redox cycling; however, an electric short circuit current was not seen. The probe−sample distance was maintained at 300 nm, which was similar to the size of aperture of the probe. From the image, the height of the Pt IDA was found to be 100 nm, which was in good agreement with the size determined by conventional AFM (Supporting Information, Figure S2). These results showed that noncontact simultaneous imaging based on topographic and electrochemical characteristics were possible on a submicrometer scale by using ion current as the feedback signal.

Enzyme Spot Measurement. The protein microarray has become a popular tool for high throughput screening of ligand−receptor binding tests. Nanoliter- to subnanoliter-sized droplets of protein solutions are arrayed on a solid surface by a robotic spotter; however, a ringlike structure at the edge of the spot[39] results in heterogeneous distribution of the protein that degrades the sensitivity and reproducibility of the protein chip. Revealing the localized activity of the enzyme spot would improve the sensitivity and reproducibility of the protein microarray. In the past, patterned monolayer enzyme activity[2] and ringlike structure at the edge of the spot[3] were measured by SECM. Especially, the Schuhmann group reported on enzyme−polymer spots,[4−6] but SECM image resolutions of those reports were not enough to clarify the submicro-scale activity of the localized spotted protein.

We measured a portion of the HRP and GOD spotted pattern using SECM/SICM. HRP and GOD measurements were performed in the substrate generation tip collection (GC) and feedback (FB) modes, respectively. Figure 5 shows the SECM/SICM images of a portion of a HRP spot edge in a PBS solution containing 0.50 mM $FcCH_2OH$. The potentials of the SECM Au nanoring and SICM Ag/AgCl electrodes were 50 and 200 mV, respectively. The SICM image shows a clear topographic image of the HRP spot with uneven surfaces in the center and a ring-like range at the edge. The height of the edge of HRP spot was found to be approximately 260 nm. The immobilized HRP catalyzes the reduction of H_2O_2 by $FcCH_2OH$ to form $[FcCH_2OH]^+$, which is reduced back to $FcCH_2OH$ at the SECM nanoring electrode. Before adding H_2O_2, the reduction current was not seen at all (Figure 5A right image), while the apparent reduction current of $[FcCH_2OH]^+$ was detected after addition of 0.50 mM H_2O_2(Figure 5B right image). The SECM image shows the increased reduction current, especially at the edge of the HRP spot, which is in good agreement with the topographic image obtained by SICM. The GC mode is known as a sensitive

(39) Deng, Y.; Zhu, X. Y.; Kienlen, T.; Guo, A. *J. Am. Chem. Soc.* **2006**, *128*, 2768–2769.

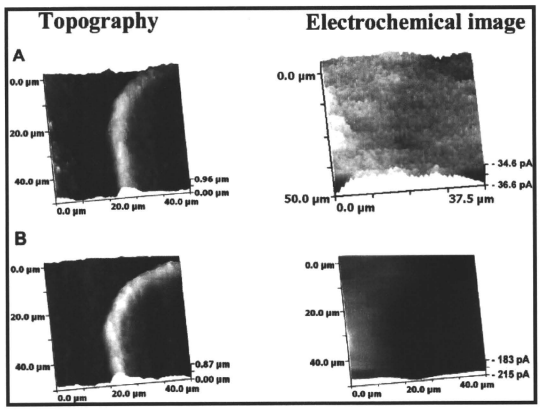

Figure 5. Topographic (left) and electrochemical (right) images of a portion of the HRP spot immobilized on a glass substrate (A) before and (B) after adding 0.50 mM H_2O_2 in 0.50 mM $FcCH_2OH$ and PBS. The SECM nanoring and SICM nanopipette electrodes were held at 50 and 300 mV vs Ag/AgCl, respectively. Scan ranges were 50 μm × 50 μm.

detection mode because the generation of the redox reaction species is dominated by enzyme activity and the background current is very low. However, it is difficult to improve the spatial resolution using a distance regulation system, even if the microelectrode is positioned near the enzyme, because the steady-state diffusion layer is formed around the enzyme. Therefore, we also performed the FB mode measurement to obtain high-resolution SECM images of enzyme spots. Feature and advantage of enzyme measurement using GC mode and FB mode was reported by Wittstock.[1]

Figure 6 shows the SECM/SICM images of a portion of the GOD spot in a PBS solution containing 0.50 mM $FcCH_2OH$. The potentials of the SECM Pt nanoring and SICM Ag/AgCl electrodes were 500 and 200 mV, respectively. At the SECM nanoring electrode, $FcCH_2OH$ is oxidized to $[FcCH_2OH]^+$, which diffuses to the surface of the GOD spot. GOD on the substrate catalyzes the oxidation of glucose and the reduction of $[FcCH_2OH]^+$ to $FcCH_2OH$ diffusing back to the SECM. When the electrode is near the GOD, redox cycling of $[FcCH_2OH]^+/FcCH_2OH$ occurred to amplify the electrochemical current. Panels A and B of Figure 6 show the SICM and SECM images before adding glucose. The topographic image from SICM indicates the ringlike structure of the GOD spot with an edge height of approximately 200 nm. The SECM image without glucose showed small differences in the oxidation current along the edge, probably due to negative feedback caused by the edge. Figure 6C shows the SECM images after adding 20 mM glucose. The increase in $FcCH_2OH$ oxidation current associated with GOD-catalyzed reaction was seen, and the electrochemical current profile was in good agreement with the topographic image of the GOD spot.

We also investigated interference between the SECM nanoring and SICM Ag/AgCl electrodes. Figure 6D shows the SECM image when the potential of the Ag/AgCl electrode changed from 200 to −200 mV, while the potential of the SECM nanoring electrode was unchanged at +500 mV. No difference in the SECM image was found before and after changing the potential of the Ag/AgCl electrode (Figures 6C and D). This indicated that the SECM nanoring and SICM Ag/AgCl electrodes had no interference.

The probe−sample distance was an important parameter for FB mode imaging. Figure 7 shows the SICM topographic and SECM images in which the probe−sample distances were held at 100 and 600 nm. The SICM image showed a highly resolved structure of the GOD spot surface with small caves 320 nm × 1600 nm in size (Figure 7A). When the distance was set to 100 nm, the SECM image also shows that fine structure with small caves (Figure 7B), but the cave-like structure disappeared in the SECM image at a distance of 600 nm (Figure 7C). These results clearly demonstrate that SICM distance regulation is very effective in improving its resolution in FB imaging. The SECM image with a higher magnification (Figure 7E) clearly shows the single cave with low electrochemical responses. Although the electrode diameter was approximately 700 nm, features as small as 100 nm could be visualized by both SICM topography and SECM images. This is the first time that the enzyme activity has been imaged with nanometer resolution using SECM.

Topographic Imaging of Live Cells. The distribution of ion channels and receptors at specific locations on the cell surface plays an important role in signal transduction. Most cell types develop complex structures that form predominant locations for ion channel and receptor clustering. Mapping the distributions of ion channels and receptors on complex surfaces by SECM would not be possible without precise distance control. Therefore, we chose two highly structured cell types, superior cervical ganglion (SCG) cells and A6 cells, to evaluate the topographical resolution of SECM/SICM. Panels A−D of Figure 8 show the optical microscopy image and topographic images of SCG cells. The red square frame of the optical microscopy image shows the scanning area of Figure 8B. By adopting the hopping mode, SECM/SICM could simultaneously image the axon and cell body. Moreover, varicosities, which administrate neuron transduction and axon formation, were seen clearly on the axon (marked by asterisks). D and E of Figure 8 show the topographic images of A6 cells. Ridge-like structures, formed by microvilli, can be seen on the cell surface.

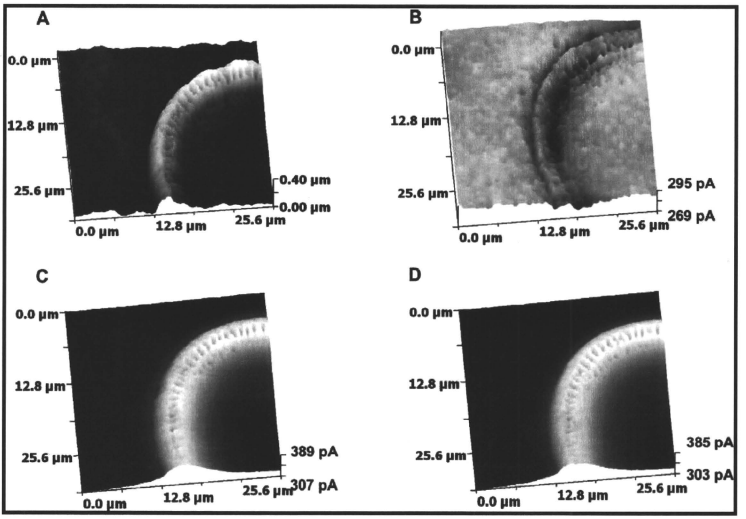

Figure 6. (A) Topographic and (B−D) electrochemical images of GOD immobilized substrate (A and B) before and (C and D) after adding 20 mM glucose in 0.50 mM $FcCH_2OH$ + 0.1 M KCl. The SECM nanoring and SICM nanopipette electrodes were held at 500 and 200 mV vs Ag/AgCl, respectively, for (A−C), while the potential of the SICM nanopipette electrode was changed to −200 mV vs Ag/AgCl for (D). Scan ranges were 32 μm × 32 μm.

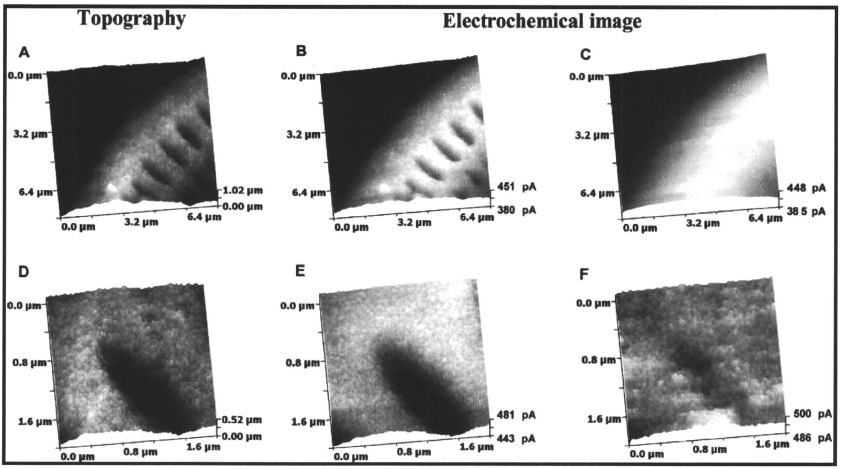

Figure 7. (A and D) Topographic and (B, C, E, and F) electrochemical images of a GOD immobilized substrate adding 20 mM glucose in 0.50 mM $FcCH_2OH$ + 0.1 M KCl. The SECM nanoring and SICM nanopipette electrodes were held at 500 and 200 mV vs Ag/AgCl, respectively. Upper and lower images were captured with 8 μm × 8 μm and 2 μm × 2 μm, respectively. The probe−sample distances were held at 100 nm (B and E) and 600 nm (C and F), respectively.

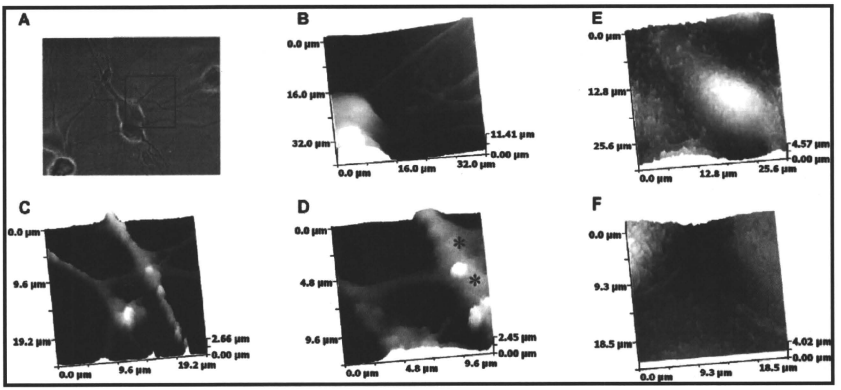

Figure 8. (A) Photograph and SICM topographic images of (B−C) SCG cells and (D, E) A6 cells in a culture medium L-15, using a SECM/SICM probe. Scan ranges were (B) 40 μm × 40 μm, (C) 24 μm × 24 μm, (D) 12 μm × 12 μm, (E) 32 μm × 32 μm, and (F) 23.1 μm × 23.1 μm.

At the cell−cell contact region, a tight junction area formed by the double row of microvilli can be seen. This is an important feature for maintaining the function of renal cells. These results indicated that the SECM/SICM probe can resolve the topography of the living cellular surface well beyond submicrometer resolution, and the hopping mode is a suitable SECM distance control for convoluted cell topography imaging.

Evaluation of Permeation Property of the Cell Membrane. The permeation property of the cell membrane plays an important role in intracellular biochemical reactions. SECM is a powerful tool for estimating transport rates of electrochemical species across the liquid/liquid interfaces.[10] Mirkin and other groups reported about electrochemical mediator permeability and electron transfer kinetics of living cells using SECM.[9,11−18] However, several technical challenges still remain unsolved. First, the cell membrane has the possibility of heterogeneous permeability in specific regions; second, biomolecules adsorb to the electrode surface (electrode fouling) and decrease the steady-state current; third, the heterogeneity of the cellular surface affects the approach curve measurement. Most simulations for estimating permeability by fitting experimental data do not consider the surface heterogeneity. It is desirable to acquire an estimation of membrane permeability with the surface topography and continually monitor the approach curves. By adopting the hopping mode, SECM/SICM can acquire the approach curve at each measurement point. Therefore, we evaluated the permeation property on the cell membrane simultaneously with the cell surface topography.

In this experiment, we measured Faradaic current for the oxygen, potassium hexacyanoferrate (II) trihydrate ($K_4[Fe(CN)_6]$), and $FcCH_2OH$ on a cardiac myocyte. Figure 9 shows the SICM topographic and SECM images and current profiles at each measurement point on a cardiac myocyte. The arrow shows a direction of the approach, from a start point (10 μm above the surface) to the sample surface (300 nm from the surface), which is the end point of the vertical scan. Unfortunately, the topographical resolution of the images was inadequate to visualize the sarcoma structure in detail; however, it was sufficient to visualize the cardiac myocyte shape very clearly. The cell height was found to exceed 20 μm. The hopping mode was effective for such high aspect sample topographic measurements. The electrochemical images were shown as a Faradaic current associated with the localized permeation property of a specific chemical. The reduction current of the oxygen (negative value) decreased as the probe approached the sample surface, indicating that the negative feedback effects were seen weakly at the all measuring points. The oxygen reduction current at the cellular membrane surface (3.6 μm < X < 7.0 μm) was clearly large compared with that at the surface of the culture dish (X < 3.6 μm; 7.0 μm < X) (Figure 9A right image). This indicated that the cell membrane has a high permeability for oxygen. It is noteworthy that the current contrast changed, depending on the SECM probe electrode size and the probe scanning rate.[22] Therefore, a very small electrode is preferential to separately characterize the local oxygen concentration and the membrane permeation property.[8]

When monitoring $[Fe(CN)_6]^{4-}$ oxidation current (positive value), the oxidation current decreases as the probe repeatedly approaches the sample surface, due to the negative feedback effects. $[Fe(CN)_6]^{4-/3-}$ is a hydrophilic mediator and cannot cross the cell membrane. At the end point of the vertical scans, the oxidation currents were seen at the same level for a cellular surface and substrate (Figure 9B right image). This indicates that the diffusion of $[Fe(CN)_6]^{4-}$ was blocked by both the cellular membrane and the substrate. At the cell edge, some strong negative feedback effect was seen. This is because the cell edge only partially blocked the diffusion of the $[Fe(CN)_6]^{4-}$. SECM/SICM can detect the electrochemical current response produced by the surface heterogeneity. $FcCH_2OH$ is a hydrophobic mediator that can cross the cell membrane.[18] When monitoring the oxidation current of $FcCH_2OH$ (positive value), the current decreased as the probe approached the sample surface, due to the slight negative feedback effects. However, similar to oxygen, the $FcCH_2OH$ oxidation current at the cellular membrane surface was large, compared to that at the substrate surface, because the cellular membrane is permeable for $FcCH_2OH$ (Figure 9C right image). The larger oxidation current may also be caused by regeneration of $FcCH_2OH$ inside the cellular processes.[7] The possibility of steady-state diffusion layer of